Available online at www.sciencedirect.com
ScienceDirect
Trans. Nonferrous Met. Soc. China 35(2025) 832−848
Transactions of Nonferrous Metals Society of China
www.tnmsc.cn

Electrochemical behavior and discharge performance of as-rolled precipitate-free Mg−Sn alloy as anode for Mg−air batteries

Xu LI[1], Wei-li CHENG[1,2], Jian LI[2], Fei-er SHANGGUAN[1], Hui YU[3], Li-fei WANG[1], Hang LI[1], Hong-xia WANG[1], Jin-hui WANG[2], Hua HOU[4]

1. School of Materials Science and Engineering, Taiyuan University of Technology, Taiyuan 030024, China;
2. The Open Project of Salt Lake Chemical Engineering Research Complex, Qinghai University, Xining 810016, China;
3. School of Materials Science and Engineering, Hebei University of Technology, Tianjin 300132, China;
4. School of Materials Science and Engineering, North University of China, Taiyuan 030051, China

Received 13 July 2023; accepted 28 February 2024

Abstract: A novel precipitate-free Mg−0.1Sn anode with a homogeneous equal-axis grain structure was developed and rolled successfully at 573 K. Electrochemical test results indicate that the Mg−0.1Sn alloy exhibits enhanced anode dissolution kinetics. A Mg−air battery prepared using this anode exhibits a cell voltage of 1.626 V at 0.5 mA/cm^2, reasonable anodic efficiency of 58.17%, and good specific energy of 1730.96 mW·h/g at 10 mA/cm^2. This performance is attributed to the effective reactive anode surface, the suppressed chunk effect, and weak self-corrosion owing to the homogeneous basal texture.

Key words: Mg−air battery; Mg−Sn anode; grain structure; electrochemical behavior; discharge performance

1 Introduction

Mg−air batteries are considered an excellent energy storage technology owing to their high theoretical voltage (3.1 V) and energy density (6.8 kW·h/kg) at an acceptably low cost [1,2]. However, because of the negative difference effect (NDE), namely severe self-corrosion, the hydrogen evolution (HE) rate of Mg anodes increases rapidly with increasing discharge time and applied current density, thus deteriorating battery performance [3,4]. The self-corrosion of Mg involves two distinct processes: electrochemical dissolution of the substrate and detachment of metallic pieces from the anode surface, which is commonly referred to as the chunk effect (CE) [5]. Furthermore, corrosion products that form on the anode surface create a film that hinders the transport of Mg^{2+} ions, thus decreasing the reactive active area on the electrode surface and resulting in voltage recession [6]. Therefore, further research efforts are required to enhance the performance of Mg anodes by modifying the internal microstructure and optimizing the effective reaction area on the anode while preventing severe self-corrosion.

Alloying and hot plastic deformation are effective strategies for enhancing the performance of Mg anodes by optimizing the internal microstructure and film of discharge products [2]. Alloying Mg by incorporating rare-earth (RE) elements can alleviate the self-corrosion of Mg anodes by refining the grain structure and facilitating the formation of protective films on the corroded surface [7]. For example, MA et al [8] reported that a Mg−5La anode exhibited a specific discharge capacity of 1259.45 mA·h/g at a current density of 20 mA/cm^2, with an anodic efficiency of

Corresponding author: Wei-li CHENG, Tel: +86-18636612588, E-mail: chengweili7@126.com
DOI: https://doi.org/10.1016/S1003-6326(24)66717-8

57.67%. This was attributed to the even distribution of a reticular $LaMg_{12}$ phase throughout the matrix. However, improving the discharge activity of Mg−RE-based anodes is highly challenging.

Non-RE alloying elements, including Zn, Pb, Al, Li, In and Ca, have been extensively used to enhance the discharge performance of Mg anodes by modifying the anodic kinetics and/or active electrode area [4,8−11]. The main limitations of these Mg alloys are their poor balance between corrosion properties and discharge activity. Furthermore, a high level of alloying leads to the precipitation of second-phase particles, which play various roles in the discharge process. Most second-phase metals are less reactive than the Mg matrix, leading to the preferential dissolution of the surrounding Mg matrix and accelerating the microgalvanic effect, thereby decreasing the utilization efficiency [12]. To date, a strong synergy between the corrosion resistance and activity using high-alloyed Mg anodes has not yet been achieved.

Numerous recent studies have reported that low-alloyed Mg−Bi and Mg−Ca-based anodes exhibit a high discharge potential, utilization efficiency, and capacity owing to a refined grain structure and limited distribution of small particles in the grain interior [13−15]. This suggests that a lean alloying design concept can overcome the issues caused by the presence of second-phase particles and improve the anode performance.

In principle, Sn can provide a high volumetric energy density (7.413 W·h/g), hydrogen over-potential, and low migration barrier (0.497 eV) for a single Mg atom [16]. Therefore, Sn is the preferred alloying element for improving the performance of Mg anodes. Our previous work proved that a Mg−Sn-based anode could exhibit an excellent discharge activity and a relatively high volume capacity, while forming a dense protective film of discharge products [17]. In addition, Sn facilitates the activation of the Mg anode dissolution−redeposition mechanism. A previous investigation of Mg anodes alloyed with Sn focused mainly on the effects of second phases, grain size, and dislocations on the discharge behavior of wrought samples [18]. However, a high Sn content can easily introduce a substantial amount of the Mg_2Sn phase, leading to the preferential dissolution of the surrounding Mg matrix and accelerating the microgalvanic effect, resulting in the CE, particularly at low current densities [19,20]. Furthermore, YU et al [21] showed that decreasing the Sn content increases the specific energy in Mg−air batteries. Therefore, a lean alloying strategy is considered to be effective for alleviating the adverse effects caused by the Mg_2Sn second phase.

Based on this background, this study developed a novel Mg−0.1Sn anode that was subjected to rolling and annealing to achieve a precipitate-free and refined grain structure with a low dislocation density. The influence of the grain structure on the electrochemical behavior and discharge performance of the alloy was examined. In addition, this study comparatively analyzed the electrochemical behavior and discharge performance between recast pure Mg and the Mg−0.1Sn alloy. The findings of this study are valuable for developing highly activated and utilization-efficient Mg anodes for application in Mg−air batteries.

2 Experimental

2.1 Material preparation

A Mg−0.1Sn (wt.%) (T0) alloy ingot was obtained by melting pure Mg and Sn (Zhongnuo Advanced Material Technology, Beijing) in a resistance furnace in a CO_2 and SF_6 mixed gas atmosphere at 1023 K to prevent oxidation. The billet (100 mm × 120 mm × 10 mm) was homogenized at 773 K for 3 h and then cooled in air. Subsequently, a lab-scale rolling mill with a 350 mm roll diameter and a rolling speed of approximately 130 mm/s was used for hot-rolling experiments. The billet was rolled for five passes at 573 K to decrease the thickness from 10.0 to 4.0 mm. Finally, the rolled alloy was annealed at 523 K for 10 min.

2.2 Microstructure characterization

The precipitate phase, microstructure, and texture of the rolled Mg−0.1Sn alloy were analyzed using scanning electron microscopy (SEM; Mira 3XMU) with energy-dispersive X-ray spectroscopy (EDS), X-ray diffraction (XRD; Bruker D8 Discover), and electron backscatter diffraction (EBSD; JEOL JSM−7000F). SEM was performed under backscattered electron (BSE) conditions. The samples were ground using SiC sandpaper up to 4000# grit before being polished with a 4 vol.%

nitric acid alcohol solution to reveal the grain boundaries. For the EBSD studies, before electrolytic polishing, the samples were ground thoroughly with SiC sandpaper up to 7000# and analyzed using HKL Channel 5 software to obtain the corresponding data.

2.3 Density functional theory calculation

The Vienna Ab initio Simulation Package (VASP) and van der Waals (DFT-D3) corrections were employed to perform first-principles density functional theory (DFT) calculations. The binding energies (E_s) of an additional Mg atom on Mg(002), Mg(100), and Mg(101) surfaces, as well as the energies required to remove a surface atom from these same surfaces, were calculated using the following formula:

$$E_s=E_{hkl-1}+E_{Mg1}-E_{hkl} \quad (1)$$

where E_{hkl-1} denotes the overall energy of the Mg surface with an adsorbed Mg atom (the removal energy is the total energy of the complete Mg surface), E_{hkl} is the energy of the Mg surfaces with different crystal planes, and E_{Mg1} represents the energy of a Mg atom. The crystal structure of Mg was modeled in a 3×3×1 supercell with a 15 Å vacuum layer. The Mg atoms were placed in a framework with the same lattice parameter as Mg(*hkl*) to prevent interference from periodic calculations. The Mg atoms were fixed at specific positions on the Mg(*hkl*) surface, with the bottom two layers fixed and the top layer relaxed. The cutoff energy for the calculations was established at 400 eV, while the tolerance for geometry optimization convergence was set to be 1.0×10^{-5} eV/atom. The maximum force and displacement were set to be 2.0×10^{-2} eV/Å and 1.0×10^{-3} Å, respectively.

2.4 Electrochemical measurement

Open-circuit potentials (OCPs), potentiodynamic polarization (PDP), and electrochemical impedance spectroscopy (EIS) of the rolled Mg−0.1Sn alloy in NaCl solution (3.5 wt.%) were conducted using an electrochemical workstation (CorrTest, Wuhan, China). The standard three-electrode cell configuration was employed, with the Mg−0.1Sn alloy sample serving as the working electrode, a platinum sheet (DJS-1DF, Shanghai, China) as the counter electrode, and a saturated calomel electrode (SCE) (containing 30 mL of distilled water, 1 g of KCl, and 1 g of agar) as the reference electrode. To achieve a stable OCP, the sample (with a test area of 1 cm^2) was immersed in a testing medium (250 mL of NaCl solution (3.5 wt.%)) in a four-necked flask for 60 min before performing the PDP and EIS measurements. The PDP was measured at a scan rate of 0.5 mV/s, with the potential range sweeping from a low voltage (−2.0 V vs SCE) to the OCP and from the OCP to a high voltage (−1.0 V vs SCE). EIS was performed using a 10 mV perturbation amplitude and frequencies from 100 kHz to 10 MHz. Electrochemical parameters were obtained by fitting the EIS results to an equivalent circuit using ZView2 software.

The HE method is a widely accepted technique for assessing the self-corrosion rate of an alloy. A simple device was prepared by placing the alloy sample with an exposed area of 1 cm^2 under an inverted conical funnel connected to a 50 mL burette (0.1 mL scale). The device was placed in a measuring tube containing 1000 mL of 3.5 wt.% NaCl solution. Hydrogen gas was collected during the constant current discharge using the same setup as that described by CHEN et al [13]. The evolved gas was measured by chronopotentiometry at various current densities (0.5, 2.5, 5.0, and 10.0 mA/cm^2) for a duration of 120 min. The experiments were repeated thrice to ensure the accuracy of the results.

2.5 Mg−air battery test

The discharge performance was characterized using an air cathode with a MnO_2/C catalyst, a 3.5 wt.% NaCl solution as the electrolyte, and a Mg−0.1Sn alloy anode, using a NEWWARE cell testing system (CT-4008T-5V6A-S1). The exposed area of the sample (1 cm^2) was polished before the discharge tests that were conducted at varying current densities to evaluate the battery characteristics. After the discharge process, each sample was sprayed with alcohol and dried in air. Subsequently, the surface morphology of the retained corrosion products was studied using SEM. After testing, these corrosion products were then removed from the alloy surface using a chromic acid solution (6 g of CrO_3 in 30 mL of distilled water), following which the anode efficiency, specific capacity, and specific energy were determined. SEM was also used to investigate the

surface morphology of the sample after the corrosion products were removed. Additionally, the composition of the corrosion product powder collected immediately after discharge testing was determined using X-ray photoelectron spectroscopy (XPS: K-Alpha). For this purpose, the sample was prepared by rinsing the discharge products obtained after a 10 h-discharge at a current density of 10 mA/cm^2 with alcohol, drying them immediately, and peeling them off quickly with a clean glass rod. The obtained data were analyzed using Avantage software.

3 Results and discussion

3.1 Microstructures

SEM image and corresponding EDS results as well as XRD pattern of the T0 alloy are shown in Fig. 1. Only a single α-Mg phase is observed. Notably, the XRD peak corresponding to the Mg(0002) surface is quite strong owing to the close-packed hexagonal crystal structure of the matrix [21].

The crystallographic orientation map (Fig. 2(a)) shows that the studied alloy has a homogeneous equiaxial grain structure, with an average grain size of 7.59 μm. Moreover, the (0001) pole figure (Fig. 2(b)) shows that the alloy exhibits a typical basal texture (13.75), with most of the grains parallel to the (0001) plane. In addition, the EBSD map (Fig. 2(c)) shows the presence of recrystallized regions (88.44%, blue), subgrains (11.50%, yellow), and deformed regions (0.06%, red). This is related to the dynamic recrystallization during rolling and resultant static recrystallization during annealing [22,23]. The KAM map (Fig. 2(d)), wherein the green areas correspond to subgrains and/or deformed regions, provides an indication of the homogenization level of the deformation, with an average KAM value of 0.769 for the studied alloy.

Figure 3(a) shows the surface atomic arrangement and electron equipotential surfaces of Mg(0002), Mg($1\bar{1}00$), and Mg($\bar{1}012$) drawn by VESTA. The arrangement of surface atoms on the ($\bar{1}012$) and ($1\bar{1}00$) crystal planes results in a higher atomic-level surface roughness than the (0002) arrangement. Therefore, the interfacial charge distributions on the ($\bar{1}012$) and ($1\bar{1}00$) surfaces enhance the local corrosion. By comparison, the atomic arrangement of the (0002) surface results in a smoother surface with a more uniform interfacial charge distribution. Based on the DFT results (Fig. 3(b)), removing Mg atoms from the (0002) plane requires more energy (0.8634 eV) compared to that from the ($\bar{1}012$) and ($1\bar{1}00$) planes (0.3272 and 0.0398 eV, respectively). Consequently, Mg atoms are preferentially removed from the ($\bar{1}012$) and ($1\bar{1}00$) crystal planes during oxidation.

3.2 Electrochemical behaviors

The OCP of the T0 alloy was measured in a 3.5 wt.% NaCl solution for 3600 s to investigate the change in the corrosion potential (φ_{ocp}) with the soaking time (Fig. 4(a)). The φ_{ocp} of the T0 alloy increased rapidly at first and then gradually decreased to a constant value. Generally, this fluctuation is ascribed to the formation and destruction of a film of corrosion products [24]. Figure 4(b) displays the polarization curve of the T0 alloy in the NaCl solution (3.5 wt.%), and Table 1 presents the related electrochemical parameters.

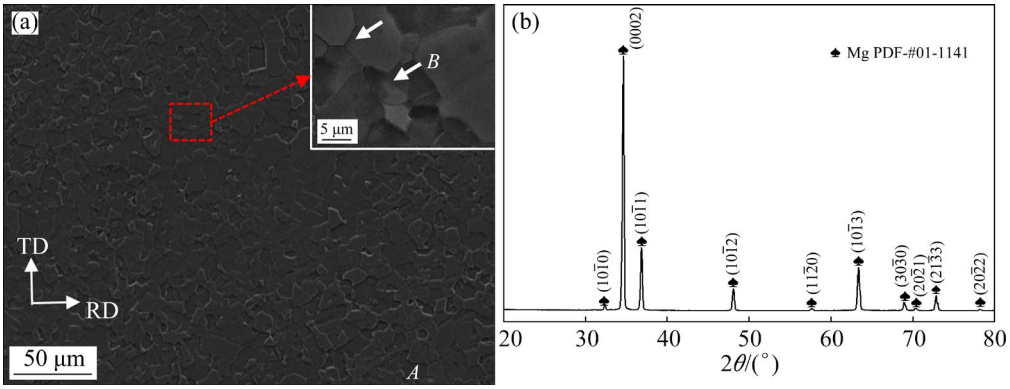

Fig. 1 SEM image (a) and XRD pattern (b) of T0 alloy

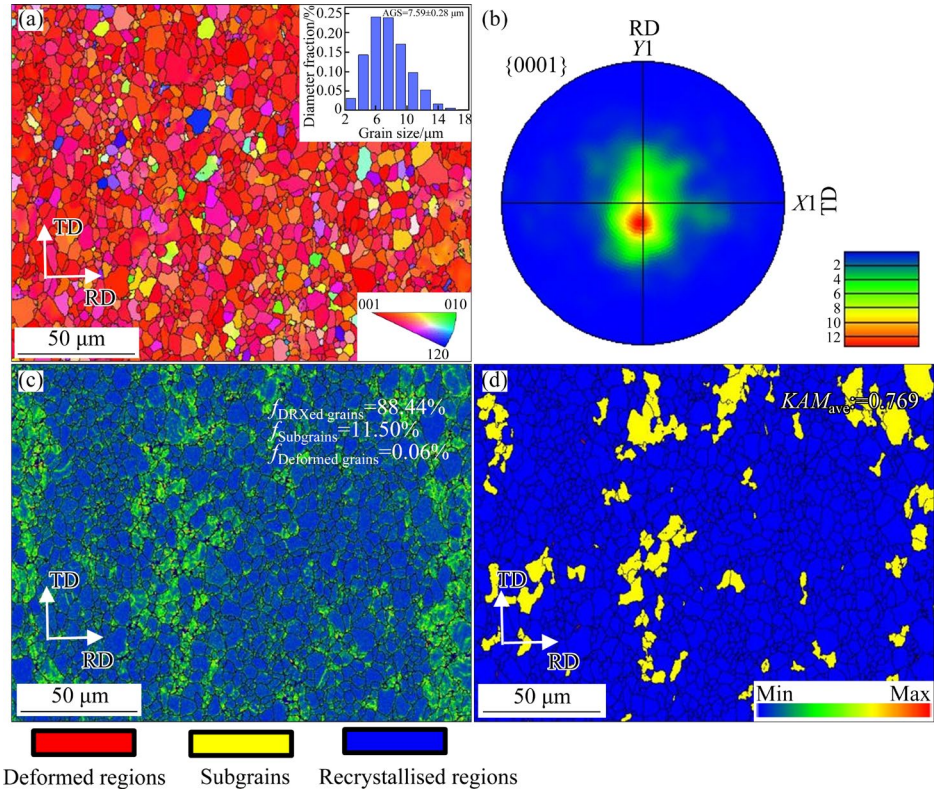

Fig. 2 Crystallographic orientation map (a), (0001) pole figure (b), EBSD map of different types of grains (c), and average kernel misorientation (KAM) map (d) of T0 alloy

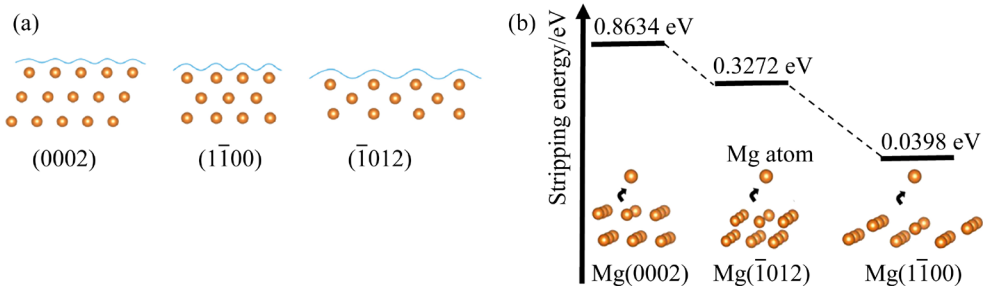

Fig. 3 Surface atomic arrangements and electron equipotential planes of Mg (0002), Mg(1$\bar{1}$00), and Mg($\bar{1}$012) (a), and stripping energy of Mg atom from different crystal planes (b)

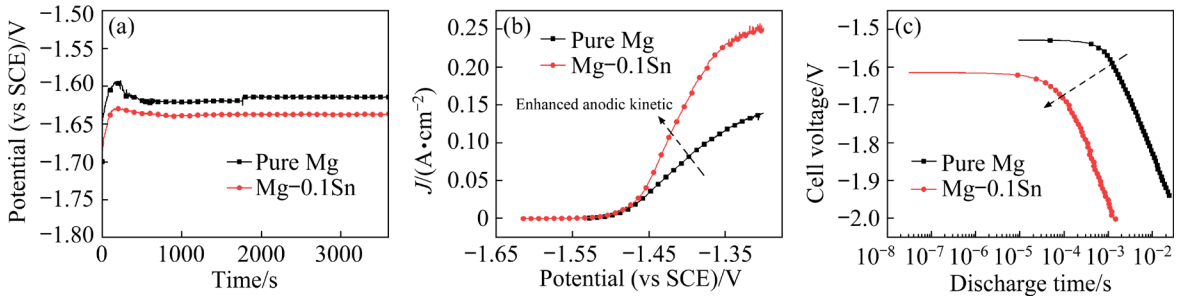

Fig. 4 OCPs (a), anodic polarization curves (b), and cathodic polarization curves (c) for pure Mg and T0 alloy

Table 1 Electrochemical parameters obtained from polarization curves

Sample	φ_{ocp}(vs SCE)/V	φ_{corr}(vs SCE)/V	β_a/mV	β_c/mV	J_{corr}/(μA·cm^{-2})	P_i/(mm·a^{-1})	R_p/(Ω·cm^2)
Pure Mg	−1.6116	−1.545	65.67	489.85	788.16	8.710	32.08
T0	−1.633	−1.615	39.93	320.68	84.17	1.923	43.717

The free corrosion potential (φ_{corr}) is related to the thermodynamic stability of the alloy, and a breach of the protective film of corrosion products results in a decrease in φ_{corr} [25]. As indicated in Table 1, the φ_{corr} of T0 is significantly lower than that of pure Mg, which indicates that Sn microalloying weakens the modification of thermodynamic stability in Mg. The polarizability of the alloy was determined by the slope of the anode curve through Tafel fitting; the slope of β_a=39.93 is larger than that of previously reported alloys [20]. This is attributed primarily to the strong basal texture of the T0 alloy which results in a high product dissolution energy during the electrode reaction process.

The current density of the anode can be expressed as an Arrhenius equation:

$$J_{anodic}=J_0\exp[-\Delta E_{vac}/(RT)] \quad (2)$$

where J_{anodic} is the current density of the anode, J_0 is the current density of pure Mg, ΔE_{vac} is the vacancy formation energy, R (8.314 J/(K·mol)) is the molar gas constant, and T (298 K) is the temperature. According to Eq. (2), J_{anodic} of corrosion is exponentially related to ΔE_{vac} [26]. In the anode, the (0001) texture provides a lower ΔE_{vac} and thus higher J_{anodic} (84.17 μA/cm^2) compared with other textures [27]. The instantaneous corrosion rate (P_i) of the T0 anode is 1.923 mm/a, indicating high electrochemical activity.

The P_i was calculated using Eq. (3) [28] as

$$P_i=22.85J_{corr} \quad (3)$$

The EIS results of the T0 alloy in the Nyquist plot at the OCP are shown in Fig. 5(a). The system exhibits multiple features at different frequency ranges, with capacitive behavior dominating at high and medium frequencies and inductive behavior dominating at low frequencies. Table 2 presents the electrochemical parameters obtained from the EIS fitting using the equivalent circuits shown in Figs. 5(b, c), where R_s is the solution resistance, R_{ct} is the charge-transfer resistance, and CPE_{dl} is the electric double-layer capacitance. In addition, R_f and CPE_f represent the resistance and capacitance, respectively, of the corrosion layer. For the T0 alloy, the series combination of the inductance L and resistance R_L indicates that the corrosion layer has decomposed, as these factors typically indicate the disruption of the surface layer and an increase in the reaction rate of the fresh uncovered metal [29,30]. Increase in R_{ct} and R_f corresponds to improvements in the resistance to corrosion [31]. Additionally, the polarization resistance (R_p) of pure Mg and the T0 alloy were separately calculated using Eq. (4) to be 32.08 and 43.717 Ω·cm^2, respectively, indicating that the T0 alloy is more resistant to corrosion than pure Mg.

$$R_p=R_s+R_f+(R_{ct}\times R_L)/(R_{ct}+R_L) \quad (4)$$

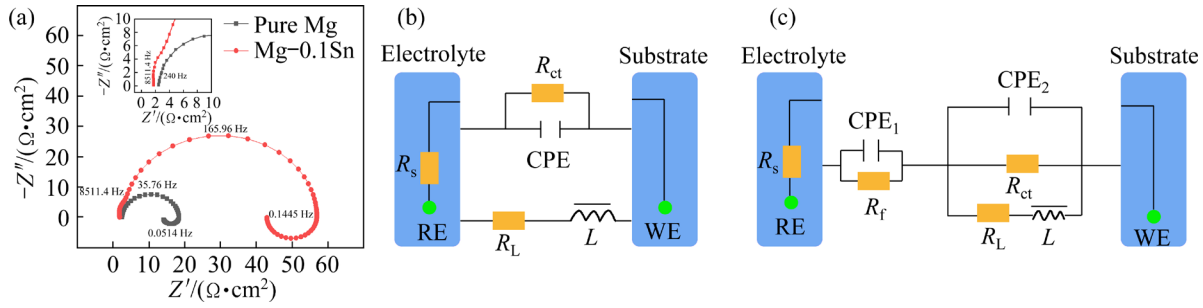

Fig. 5 EIS Nyquist plots (a) under their respective OCPs, and equivalent circuit of pure Mg (b) and Mg−0.1Sn (c) for fitting EIS of studied alloys

Table 2 Electrochemical parameters obtained from impedance parameters of studied alloy fitted by EIS

Sample	R_s/ (Ω·cm^2)	R_f/ (Ω·cm^2)	CPE_{dl-1}		R_{ct}/ (Ω·cm^2)	CPE_{dl-2}		L/ (H·cm^2)	R_L/ (Ω·cm^2)
			Y/(Ω^{-1}·cm^2·s^n)	n_{dl}		Y/(Ω^{-1}·cm^2·s^n)	n_{dl}		
Pure Mg	2.336				35	7.431×10^{-5}	0.9	50	40
T0	2.548	1.069	1.228×10^{-6}	1.3	54	8.942×10^{-6}	1	220.9	155.2

3.3 Discharge properties of Mg−air batteries

Figures 6(a−d) show the discharge curves of the T0 anode for Mg−air batteries operating at various current densities (0.5, 2.5, 5.0, and 10 mA/cm^2). The voltage decreases over time at all current densities, and then stabilizes after approximately 1 h. The voltage drop observed during the initial discharge process is attributed to the formation of the discharge product film on the T0 anode surface. Subsequently, a dynamic balance is achieved between the formation and delamination of the discharge products [32]. Figure 6(e) shows the intermittent discharge curves. The discharge voltage of the T0 anode remains stable during every discharge cycle, although the operating voltage decreases slightly after the first four cycles. By the fifth discharge cycle, the voltage decreases to approximately 1.46%. The average cell voltage and anodic efficiency at various current densities are presented in Fig. 5(f). The results show that the highest cell voltage (1.626 V) and anode efficiency (58.17%) occur at 0.5 and 10 mA/cm^2, respectively. As shown in Eq. (5), the cell voltage (V) was calculated from the open circuit voltage (OCV, V_{OC}) obtained without load, the current density (J) during the discharge process, and the total resistances of the anode (R_a), cathode (R_b), and electrolyte (R_e) [10].

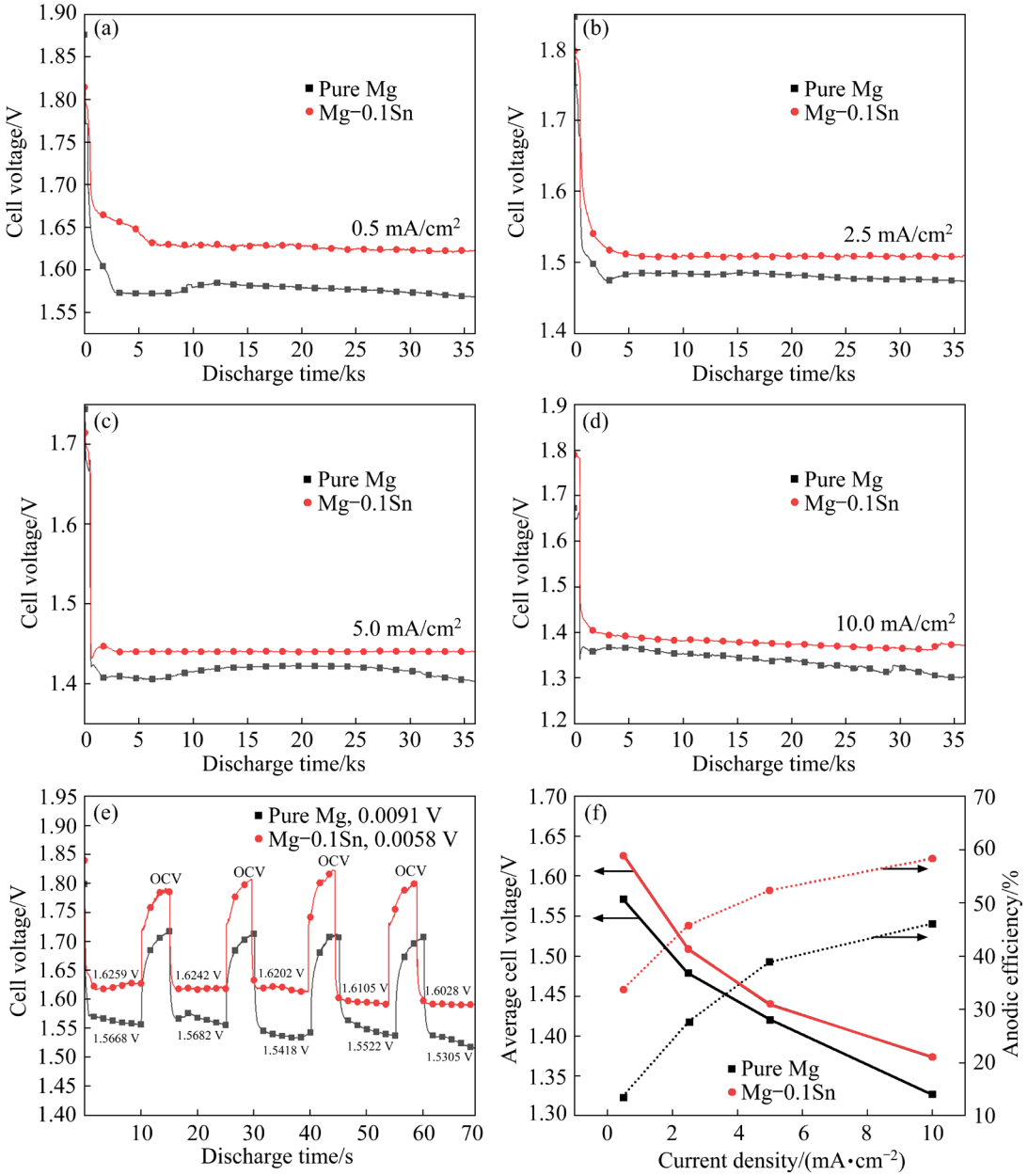

Fig. 6 Discharge curves of T0 anode at current densities of 0.5 (a), 2.5 (b), 5.0 (c) and 10.0 mA/cm^2 (d), intermittent discharge using pure Mg or T0 anodes at 0.5 mA/cm^2 (e), and average cell voltage and anodic efficiency (f)

$$V=V_{OC}-J(R_a+R_b+R_e) \quad (5)$$

Equation (5) indicates that lower J and R_a values result in higher V values because V_{oc}, R_b and R_e have similar values for the same cell arrangement. A previous work demonstrated that R_a tends to increase as the applied J increases. Hence, V is largely determined by the applied J [2].

The specific capacity and energy density of the T0 anode (Fig. 7(a)) increase with increasing current density, and the peak values are 1296.03 mA·h/g and 1730.96 mW·h/g, respectively. Intermittent discharge testing is commonly employed to simulate Mg−air battery discharge processes in practice. The findings indicated that micro-alloyed Sn maintained the effective reactive area during the discharge process, which is possibly related to the competition between the formation and shedding of the discharge product film [33]. Figure 7(b) plots the discharge voltage and efficiency values for various alloys measured at 10 mA/cm^2. The high discharge voltage and anodic efficiency of the Mg−0.1Sn alloy indicate its prospects for further advancement and application as an anode material in Mg–air batteries [3,5,10,16].

Figures 8(a−d) show that the volume of the evolved hydrogen increases with increasing current density, which could be attributed to the NDE occurring at the Mg anode [1,3]. Note that the absolute hydrogen volume of T0 anode is lower than that of pure Mg, which is possibly related to the solubilized Sn in the matrix. Sn has been reported to inhibit the self-decay of Mg alloys by

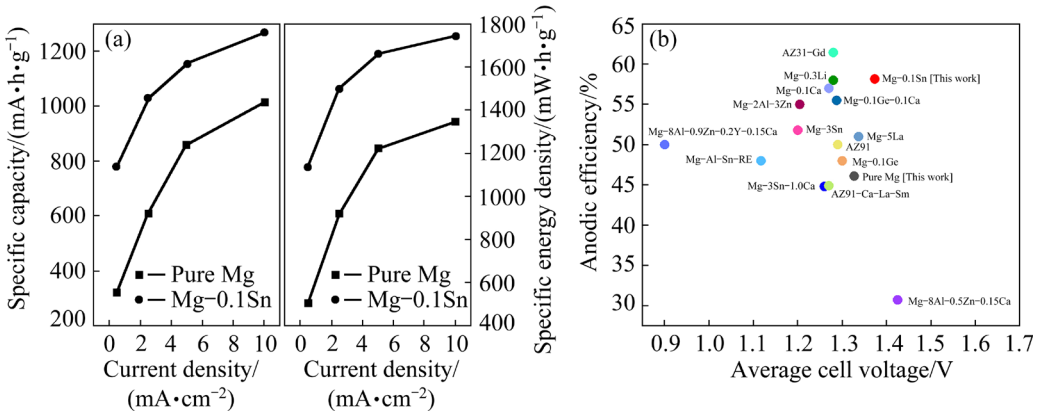

Fig. 7 Specific capacity and energy density of studied alloys (a), and comparison of discharge properties of various Mg alloys at 10.0 mA/cm^2 (b)

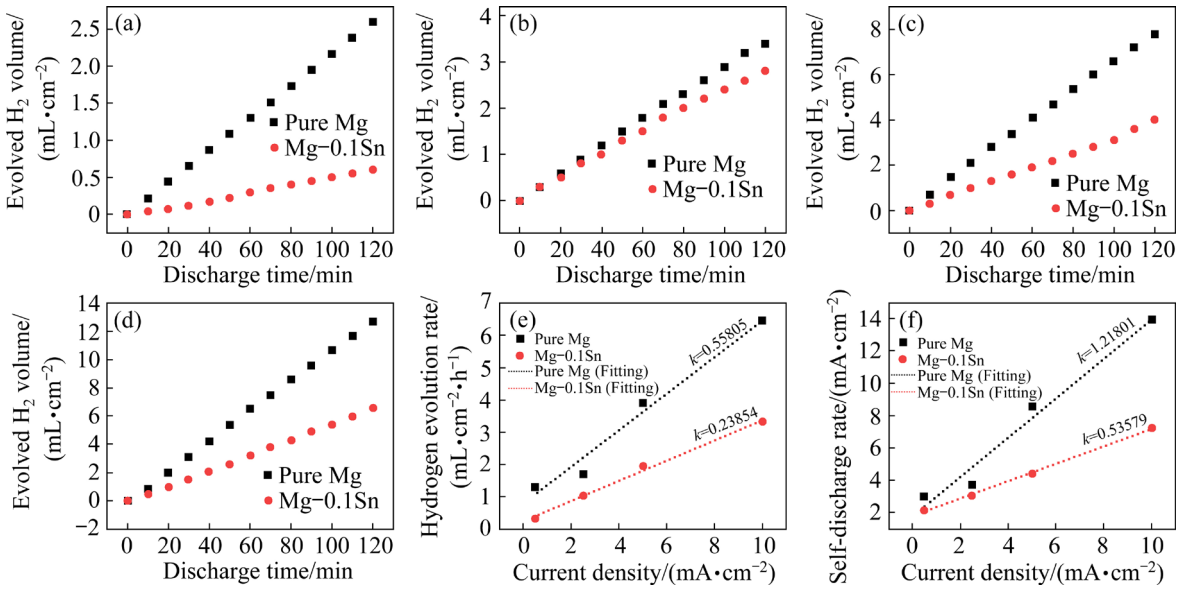

Fig. 8 Hydrogen evolution (HE) of pure Mg and T0 anode at current densities of 0.5 (a), 2.5 (b), 5.0 (c) and 10.0 mA/cm^2 (d), real-time HE rates as function of applied current density (e), and HE self-discharge rate as function of current density (f)

inducing a high hydrogen overpotential [6]. Furthermore, Figs. 8(e,f) reveal that the HE and self-discharge rates increase as the current density increases, via the Faraday's law. The slopes (k) of linear fits of the curves for the T0 and pure Mg anodes are 1.218 and 0.536, respectively, indicating that Sn alloying effectively decreases the self-discharge rate of the anode. A previous study noted that the k value of Mg alloy anodes is related to the alloy composition and microstructure [4].

Generally, the performance of Mg−air batteries in terms of their anode efficiency is dependent on two critical factors: the occurrence of the HE side reaction and the CE [4]. As illustrated in Fig. 8, the side reaction intensifies with increasing current density. Nevertheless, the highest anodic efficiency of the present anode was achieved at a high current density. Figure 9(a) shows that self-corrosion and the CE are mitigated by increasing the discharge current density, which is attributed to the basal texture being evenly distributed across the T0 anode, resulting in a low corrosion rate [28]. Overall, the anode efficiency (η) increases with increasing current density [10].

$$V_{Mg}=N_{e,a}/N_W \quad (6)$$

$$N_W=W_L/24.31 \quad (7)$$

$$N_{e,a}\approx J_{applied}/F \quad (8)$$

where V_{Mg} is the apparent valence state of Mg, $N_{e,a}$ is the electron flow related to the anodic partial reaction (mmol/(cm^2·h)), N_W is the Mg metal depletion rate during discharge (mmol/(cm^2·h)), W_L is the rate of mass loss (mg/(cm^2·h)), $J_{applied}$ is the applied current density (mA/cm^2), and F is the Faraday constant. Apparent valence values below 1.0 correspond to the loss of the Mg anode through the CE [10]. According to Fig. 9(b), the apparent valence of the T0 anode increases from 0.404 to 0.765 with increasing current density, indicating that the CE is mitigated at higher current densities because of the extensive and even dissolution process of this anode.

3.4 Surface morphologies after discharge

The phase compositions of the T0 anode after discharge were analyzed to identify the activation mechanism. According to the XPS results in Fig. 10, the primary components of the discharge products from the T0 anode are $Mg(OH)_2$ and SnO_2. Moreover, the dissolution mechanism of the T0 anode is summarized as follows [19]:

$$2Mg+O_2+2H_2O\rightarrow 2Mg(OH)_2\downarrow \quad (9)$$

$$Mg+2H_2O\rightarrow Mg(OH)_2\downarrow+H_2\uparrow \quad (10)$$

$$2Mg+Sn+4H_2O\rightarrow SnH_4+2Mg(OH)_2\downarrow \quad (11)$$

$$SnH_4+2H_2O\rightarrow SnO_2+3H_2\uparrow \quad (12)$$

$Mg(OH)_2$ precipitates primarily through the reactions in Eqs. (9) and (10), where Eq. (9) is the ideal electrode reaction [17]. Equation (10) is the HE reaction of Mg during the discharge process, which is attributed to the unavoidable NDE of Mg. Equation (11) shows that SnH_4 is formed during the reaction, but this compound is unstable at 24−26 °C (boiling point of −52 °C) [17]. Hence, SnO_2 with excellent chemical stability is obtained through the reaction in Eq. (12) [34]. As previously reported, the surface potential of the T0 matrix can be changed by the dissolution of solutes into the matrix. Sn increases the hydrogen overpotential and decreases the energy barrier to migration, thus

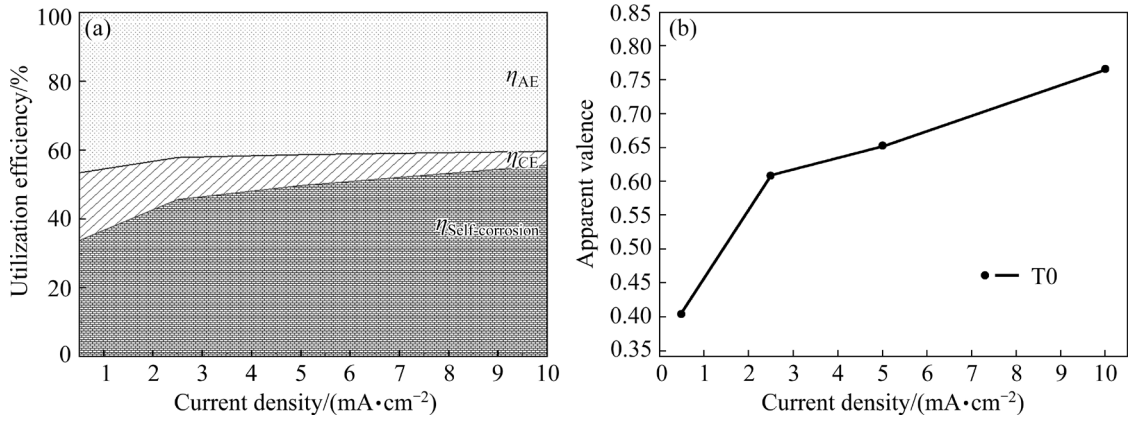

Fig. 9 Distribution of η_{AE} (actual anodic efficiency), $\eta_{Self\text{-}corrosion}$ (efficiency loss due to self-corrosion), and η_{CE} (efficiency loss due to CE) (a), and apparent valence of anodes at various current densities (b) of T0 anode

facilitating the diffusion of individual Mg atoms (0.497 eV) [16]. Therefore, Sn microalloying is effective in inhibiting the self-discharge of the anode and promoting effective solubilization for the discharge process.

The surface morphology of the T0 anode reflects the dissolution mechanism at 0.5 mA/cm^2 for different discharge time. As depicted in Fig. 11, the precipitates gradually accumulate during the discharge progress, increasing the thickness of the precipitate layer from 3.74 to 96.74 μm. Over time, the surface of the T0 anode is covered with increasing amounts of discharge products with a petal-like morphology (Figs. 11(d−i)). These petal-like products with open pores provide ion transport channels that facilitate the homogeneous dissolution of the matrix (DOM) [35,36]. Furthermore, there is a notable increase in the number of cracks on the anode surface with extended discharge time, which is attributed to an increase in the local stress concentration, which increases the effective reaction area and the discharge activity of the T0 anode.

The characteristics of the deposited layers after discharge, including the layer thickness, surface coverage, and porosity, are typically ascribed to the anode dissolution behavior and respective interfacial effects [37]. Figure 12(a) shows that the

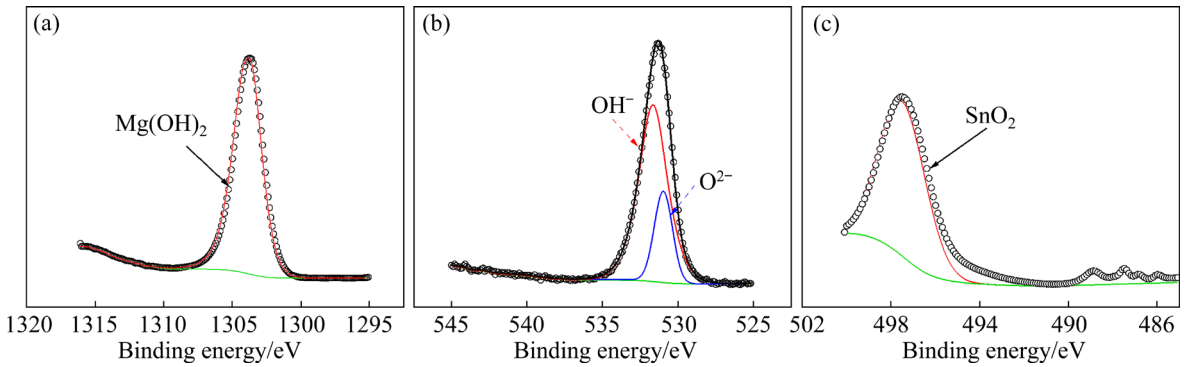

Fig. 10 XPS analysis of discharge products of T0 anode: High-resolution Mg 1s (a), O 1s (b), and Sn 3d (c) spectra

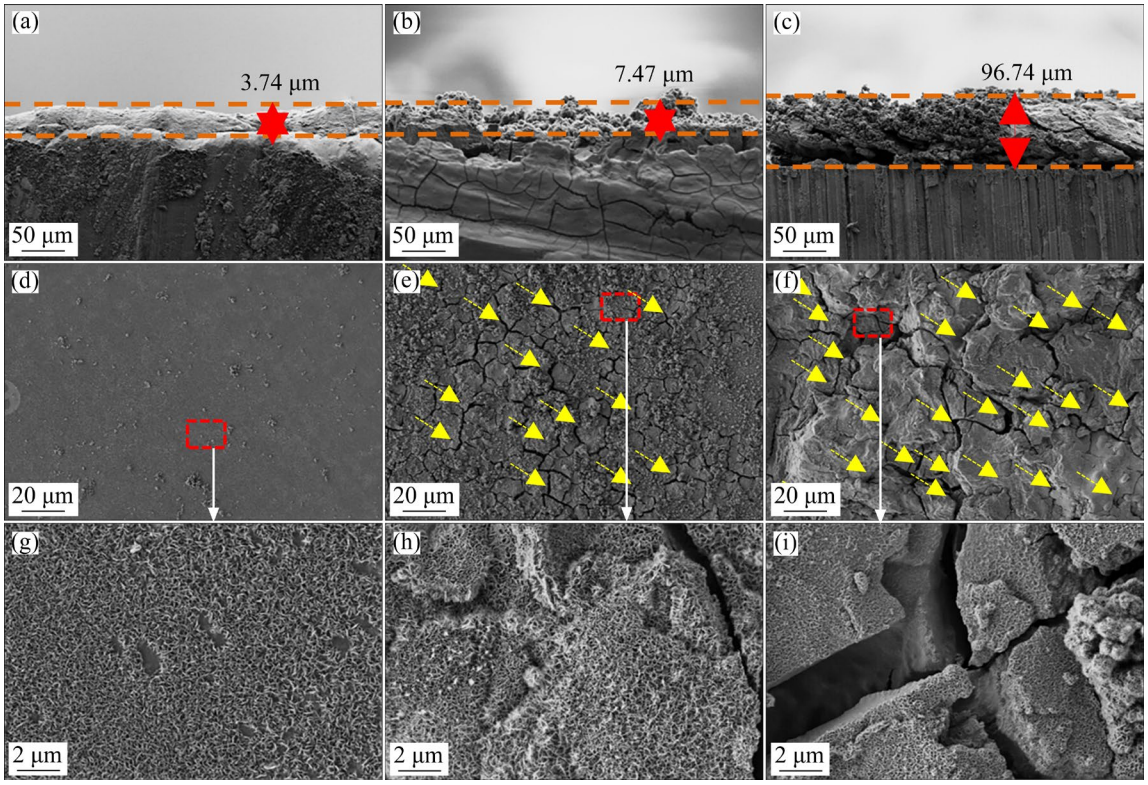

Fig. 11 SEM images of discharge product layers obtained on T0 anode showing thickness (a−c) and surface at low (d−f) and high (g−i) magnifications after 10 min (a, d, g), 30 min (b, e, h), and 10 h (c, f, i) in NaCl solution

thickness of the discharge product film gradually increases with extended discharge time and increasing current density. The surface coverage and porosity of the T0 anode were obtained by using 2D time-dependent calculation formulas of a discharging Mg anode described previously [13], the product thickness and the results are shown in Figs. 12(b,c). The surface coverage increases rapidly during the initial discharge stage, followed by a slow increase and a plateau at the maximum value. These phenomena indicate that the electron transfer resistance follows a similar trend to that of the surface coverage [37]. Figure 12(c) shows that the porosity of the deposit gradually decreases with increasing discharge time and current density due to the NDE [8]. Furthermore, the porosity of the deposit varies little with time at a low current density (0.5 mA/cm^2).

Figure 13(a) displays the EIS curves of the T0 anode as a function of the discharge time, while Fig. 13(b) depicts the corresponding equivalent circuit diagram used to fit these data. The electrochemical parameters obtained by fitting the EIS data are shown in Table 3. Only a capacitive loop is observed in the impedance diagram, the diameter of which increases over time, implying an increase in R_{ct}. This is closely related to the expanded surface coverage of the deposited layer, as shown

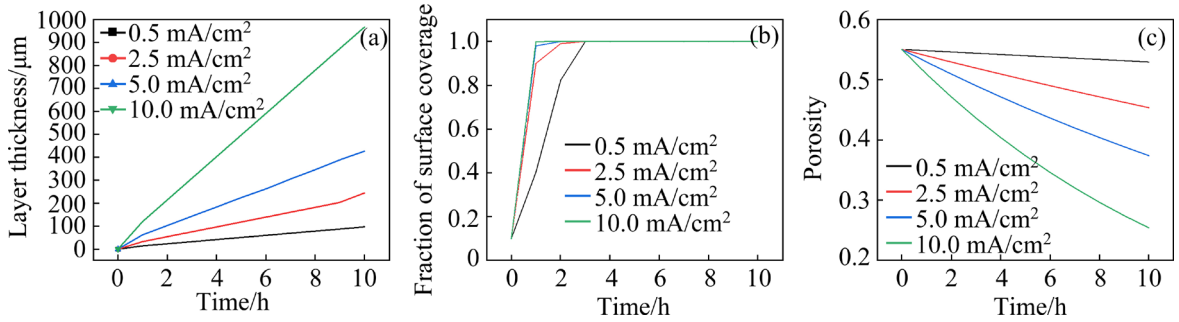

Fig. 12 Layer thickness of $Mg(OH)_2$ on T0 anode with time at various current densities (a), simulated changes of fraction of anode surface coverage with time at different current densities (b), and porosity of deposits on T0 anode with time at various current densities (c)

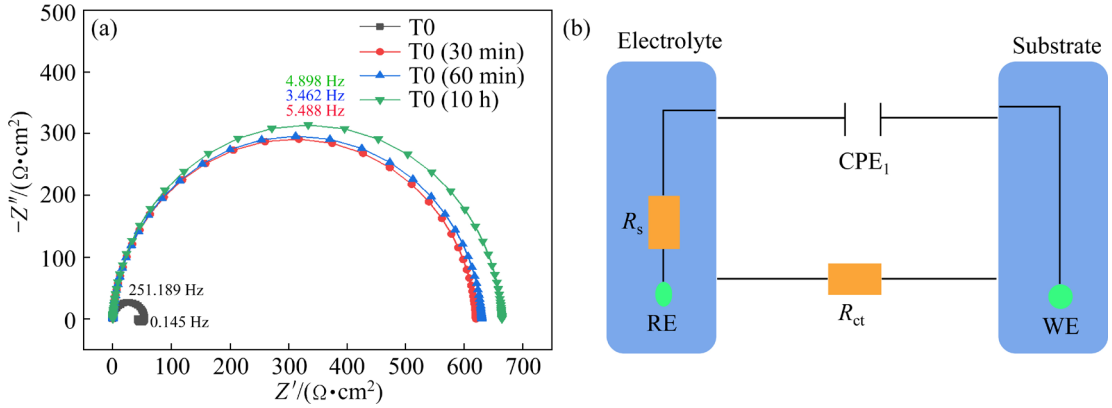

Fig. 13 Impedance plot for T0 anode measured at 0.5 mA/cm^2 after various discharge time (a), and equivalent circuit diagram used to fit these data (b)

Table 3 Electrochemical parameters obtained from impedance parameters of studied alloys fitted by EIS

Sample	R_s/ (Ω·cm^2)	R_f/ (Ω·cm^2)	CPE_{dl-1}		R_{ct}/ (Ω· cm^2)	CPE_{dl-2}		L/ (H·cm^2)	R_L/ (Ω·cm^2)
			Y/(Ω^{-1}·cm^2·s^n)	n_{dl}		Y/(Ω^{-1}·cm^2·s^n)	n_{dl}		
T0	2.548	1.069	1.228×10^{-6}	1.3	54	8.942×10^{-6}	1	220.9	155.2
T0 (30 min)	2.548				620	8.942×10^{-6}	0.94	220.9	155.2
T0 (60 min)	3.293				630	5.068×10^{-5}	0.94		
T0 (10 h)	2.421				664	2.780×10^{-5}	0.95		

in Fig. 12(b). Furthermore, the electrochemical resistance of the T0 anode is higher after discharge for 30 min compared with that of a counterpart without an applied current density, which is attributed to the rapid coverage of the surface by the precipitate layer [38]. However, the rate of increase in R_{ct} decreases considerably after the initial 30 min at 0.5 mA/cm^2, possibly because the layer porosity remains constant [5].

The pH is an important system parameter for Mg−air battery anodes during discharge because it has a significant influence on the dissolution mechanism. The φ−pH diagram (Fig. 14(a)) was derived from substances in an aqueous solution [39]. Line VI describes the trend of the φ−pH relationship for the T0 anode during 10 h of discharge. As shown in the SEM image in Fig. 11(a), $Mg(OH)_2$ precipitates begin to form after 10 min of discharge (pH=8.4), indicating that the discharge products exist predominantly in the form of Mg^{2+} and OH^-. Subsequently, the pH gradually increases

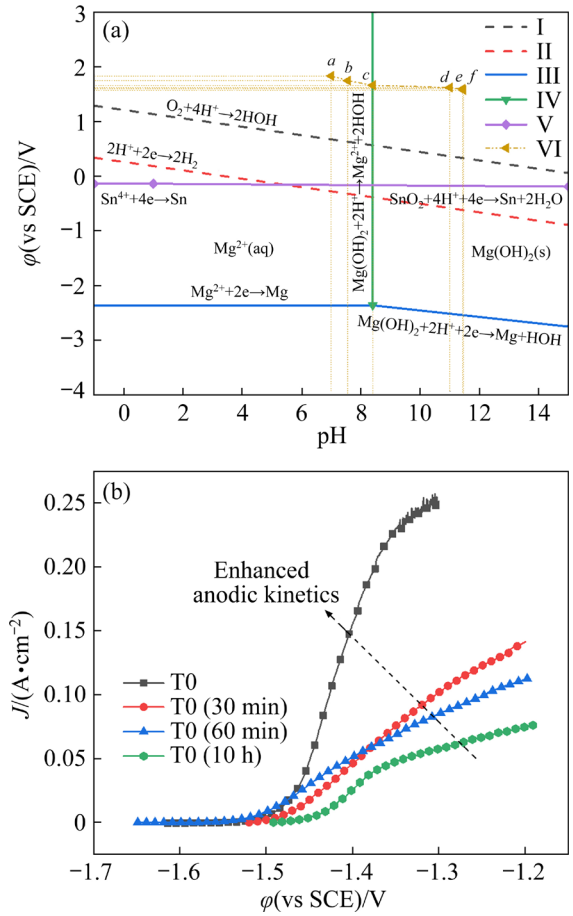

Fig. 14 Two-dimensional φ−pH diagram (a) (Points *a*–*f* indicate the conditions obtained at 0 min, 1 min, 10 min, 30 min, 1 h and 10 h, respectively, of discharge for pure Mg), and anodic branches of polarization curves (b)

to 11.43 and then remains constant, indicating that the soluble discharge products reach saturation in solution after 1 h.

The anodic branches of the polarization curves of the T0 anode are presented in Fig. 14(b), and the corresponding electrochemical parameters are shown in Table 4. Note that the anodic dynamics decrease as the discharge time increases, which is related to the accumulation of discharge product layers on the anode surface, hindering mass transport during discharge [17]. Accordingly, increase in the thickness and density of the product layer is observed (Fig. 9). These results show that the driving force for the DOM decreases with increasing discharge time. In general, the reaction kinetics are mostly related to the formation of microgalvanic cells between the grain interior and grain boundary, between basal- and non-basal-oriented regions, between dislocation and dislocation-free areas, and between the matrix and intermetallic compounds, where the potential differences provide a driving force for discharge propagation.

Table 4 Electrochemical parameters obtained from polarization curve

Sample	φ_{corr}(vs SCE)/ V	β_a/ mV	β_c/ mV	J_{corr}/ (μA·cm^{-2})
T0	−1.615	39.93	320.68	84.17
T0 (30 min)	−1.520	44.32	339.21	35.87
T0 (60 min)	−1.649	47.61	174.59	141.65
T0 (10 h)	−1.492	66.00	363.00	785.7

The discharge performance of the T0 anode at different current densities is significantly influenced by the surface morphology. As indicated by the yellow dotted arrows in Fig. 15, the number and width of cracks in the discharge product films significantly decrease with increasing current density. These results suggest that the discharge voltage decreases with increasing current density owing to the decreased reaction area and the increased resistance of the anode. In addition, at higher applied current densities, fewer deep pores at the grain boundaries of the T0 anode are observed, suggesting that the CE is weakened because cathodic reactions are less likely to occur [8].

To further investigate the discharge mechanism of the T0 anode, the surface morphologies after

various discharge time are shown in Fig. 16. Figure 16(a) shows a grain-boundary map of a T0 anode, with the low-angle grain boundaries (LAGBs; 53.2%) in red and the high-angle grain boundaries (HAGBs; 46.8%) in blue. The excess energy of LAGBs is usually much lower than that of conventional HAGBs; moreover, a high fraction of LAGBs can significantly stabilize the microstructure, thereby retarding recrystallization and promoting the recovery process to obtain very fine grains [40]. These results are attributed to the T0 anode undergoing repeated cycles of plastic deformation and recrystallization, which promotes the formation of LAGBs [41]. Furthermore, the original grains undergo reorganization during this process, ultimately leading to the formation of new, fine grain structures [42]. Consequently, during the preliminary discharge, shallow pits are homogeneously

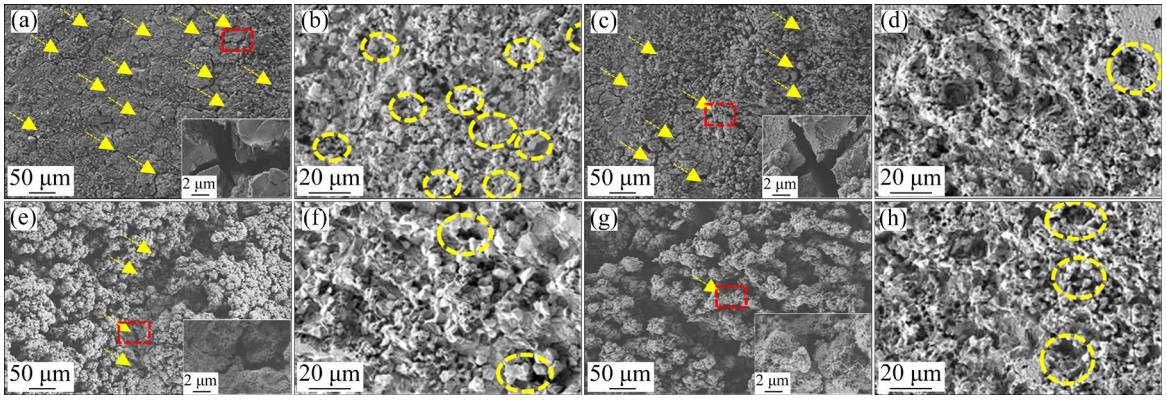

Fig. 15 Surface SEM images and locally enlarged morphologies of T0 anode after discharge for 1 h in NaCl electrolyte with (a−d) and without (e−h) discharge products and measured at current density of 0.5 (a, e), 2.5 (b, f), 5.0 (c, g), and 10 mA/cm^2 (d, h)

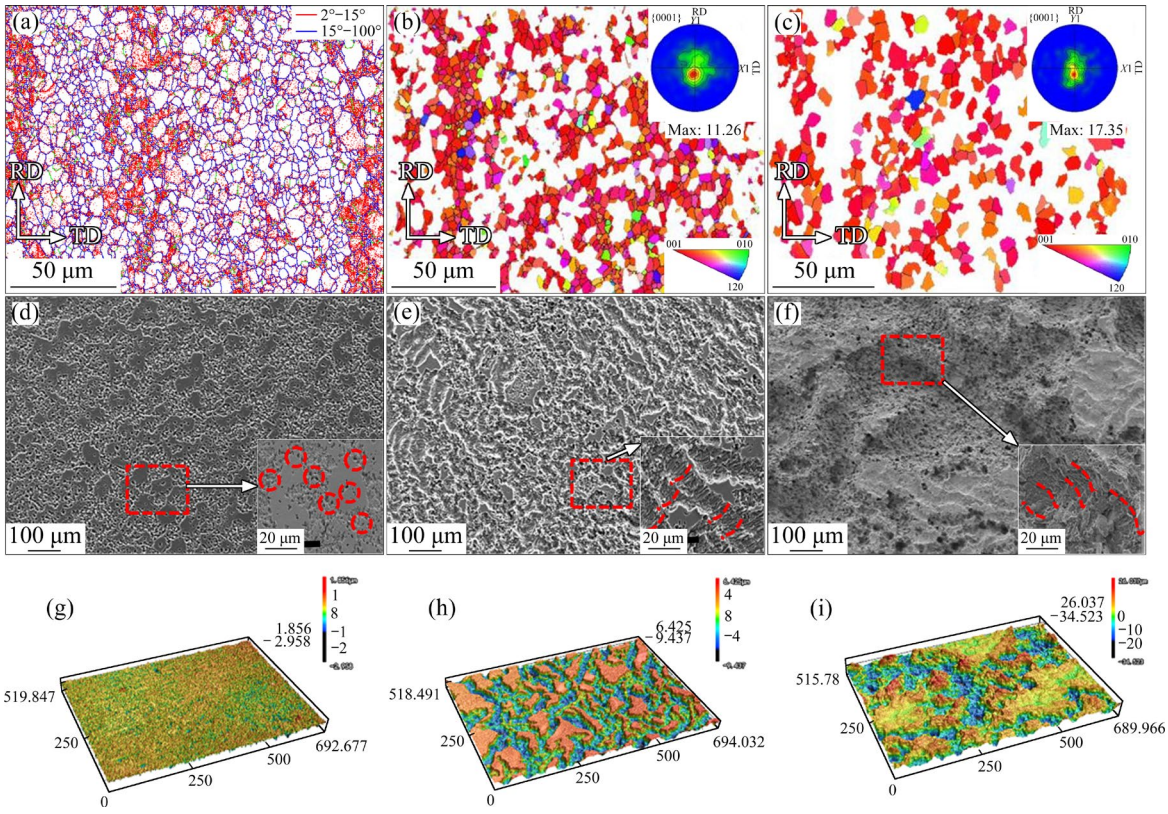

Fig. 16 Grain-boundary map of T0 anode (a), corresponding grain size distributions over range of 0−7.59 μm (b) and >7.59 μm (c), surface SEM images (d−f) and 3D morphologies (g−i) of T0 anode after removal of discharge product formed after 1 min (d, g), 1 h (e, h) and 10 h (f, i) at 0.5 mA/cm^2, respectively

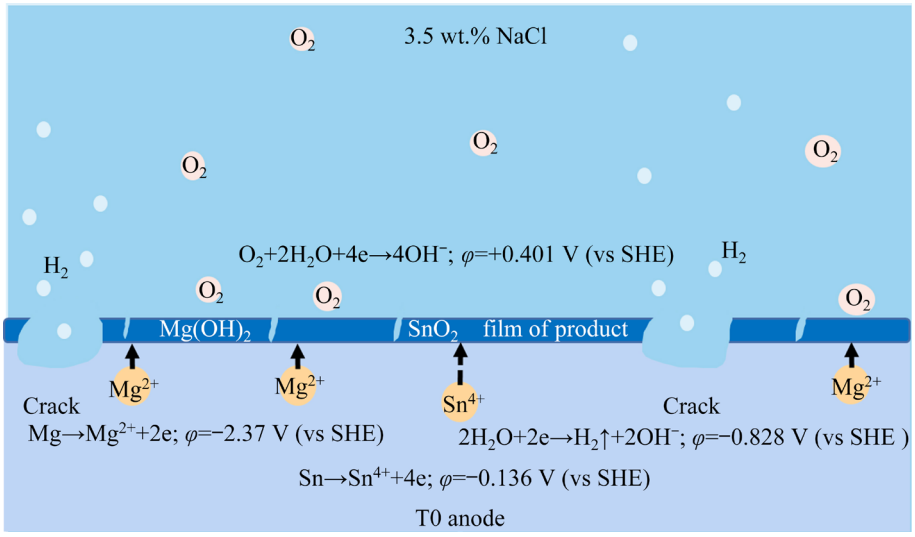

Fig. 17 Schematic of discharge process of T0 alloy as Mg−air battery anode in 3.5% NaCl solution

formed on the surface of the T0 anode (Figs. 16(d, g)). When the discharge time extends to 1 h, the corrosion pits extend laterally and link together to form long grooves (Figs. 16(e, h)). This occurs because of the strong kinetics that favor the dissolution of the fine grains distributed in the anode network [3]. When the discharge time extends to 10 h, the larger grains gradually dissolve, and the corrosion grooves expand and deepen, ultimately forming a scale-like structure on the T0 anode (Figs. 16(f, i)).

The mechanism occurring during the discharge of the T0 anode model in the NaCl solution is schematically illustrated in Fig. 17. HE occurs due to a reaction between water and the electrons generated by the DOM, which significantly decreases the number of electrons that pass through the external circuit and reach the cathode. As a result, the anodic efficiency and capacity of the T0 anode decrease. Based on our previous research [13], Mg−Bi-based alloys demonstrate superior discharge performance as anodes in Mg−air batteries compared with pure Mg. Compared to Mg−Bi-based alloys at 2.5 mA/cm^2, the T0 anode exhibits a lower rate of HE. Moreover, after a discharge time of 1 h, the T0 anode exhibits wider cracks in the product film. The deposited SnO_2 acts as a physical barrier that isolates $Mg(OH)_2$, thus contributing to the inhibition of HE during discharge [35]. Furthermore, the deposited SnO_2 promotes the generation of additional cracks and accelerates the shedding of discharge products, contributing to maintaining a large active anode area [43−47]. Finally, because O_2 has a higher potential than H_2O in the reduction reaction, HE is relatively weak [38].

4 Conclusions

(1) A novel precipitate-free Mg−0.1Sn anode with a homogeneous equiaxial grain structure and strong basal texture is fabricated by rolling and annealing. The average grain size and texture intensity are 7.59 and 13.75 μm, respectively.

(2) A Mg–air battery containing a Mg−0.1Sn anode exhibits a negative cell voltage of 1.626 V at 0.5 mA/cm^2, reasonable anodic efficiency of 58.17%, and good specific energy of 1730.96 mW·h/g at 10 mA/cm^2.

(3) This good performance is attributed to the effective reactive area of the anode surface due to the formation of SnO_2, decreased HE and suppressed CE related to the effective DOM.

CRediT authorship contribution statement

Xu LI: Investigation, Formal analysis, Writing − Original draft, Writing − Review & editing; **Wei-li CHENG**: Conceptualization, Supervision, Project administration; **Jian LI:** Funding acquisition, Resources; **Fei-er SHANGGUAN:** Validation, Formal analysis; **Hui YU:** Formal analysis, Writing − Review & editing; **Li-fei WANG**: Methodology, Writing – Review & editing; **Hang LI:** Funding acquisition, Resources; **Hong-xia WANG:** Validation, Writing − Review & editing; **Jin-hu WANG:** Conceptualization, Supervision; **Hua HOU:** Formal analysis, Writing – Review & editing.

Declaration of competing interest

The authors declare that they have no known competing financial interests or personal relationships that could have appeared to influence the work reported in this paper.

Acknowledgments

This work was partially supported by the National Natural Science Foundation of China (No. 51901153), Shanxi Scholarship Council of China (No. 2019032), the Natural Science Foundation of Shanxi, China (No. 202103021224049), and the Shanxi Zhejiang University New Materials and Chemical Research Institute Scientific Research Project, China (No. 2022SX-TD025).

References

[1] LI Shu-bo, LI Han, ZHAO Chen-chen, WANG Zhao-hui, LIU Ke, DU Wen-bo. Effects of Ca addition on microstructure, electrochemical behavior and magnesium−air battery performance of Mg−2Zn−*x*Ca alloys [J]. Journal of Electroanalytical Chemistry, 2022, 904: 115944.

[2] CHEN Xing-rui, LIU Xuan, LE Qi-chi, ZHANG Ming-xing, LIU Ming, ATRENS A. A comprehensive review of the development of magnesium anodes for primary batteries [J]. Journal of Materials Chemistry A, 2021, 9: 12367−12399.

[3] LIU Jing-jing, HU Hao, WU Tian-qi, CHEN Jin-peng, YANG Xu-sheng, WANG Nai-guang, SHI Zhi-cong. Tailoring the microstructure of Mg−Al−Sn−RE alloy via friction stir processing and the impact on its electrochemical discharge behaviour as the anode for Mg−air battery [J]. Journal of Magnesium and Alloys, 2024, 12: 1554−1565.

[4] DENG Min, WANG Lin-qian, HÖCHE D, LAMAKA S V, SNIHIROVA D, VAGHEFINAZARI B, ZHELUDKEVICH M L. Clarifying the decisive factors for utilization efficiency of Mg anodes for primary aqueous batteries [J]. Journal of Power Sources, 2019, 441: 227201.

[5] ZOU Qi, LE Qi-chi, CHEN Xing-rui, JIA Yong-hui, BAN Chun-yan, WANG Tong, WANG He-nan, GUO Rui-zhen, REN Liang, ATRENS A. The influence of Ga alloying on Mg−Al−Zn alloys as anode material for Mg−air primary batteries [J]. Electrochimica Acta, 2022, 401: 139372.

[6] JAYASAYEE K, LEÓN P D, JUEL M. Electrochemical power sources: Fundamentals, systems, and applications [M]// Alternative chemistries in primary metal−air batteries. Amsterdam: Elsevier, 2021, 4: 47−79.

[7] CHEN Xing-rui, VENEZUELA J, DARGUSCH M. The high corrosion-resistance of ultra-high purity Mg−Ge alloy and its discharge performance as anode for Mg−air battery [J]. Electrochimica Acta, 2023, 448: 142127.

[8] MA Bing-jie, TAN Cheng, OUYANG Liu-zhang, SHAO Huai-yu, WANG Nai-guang, ZHU Min. Microstructure and discharge performance of Mg−La alloys as the anodes for primary magnesium-air batteries [J]. Journal of Alloys and Compounds, 2022, 918: 165803.

[9] HUANG Dan-ya, CAO Fu-yong, YING Tao, ZHENG Da-jiang, SONG Guang-Ling. High-energy-capacity metal-air battery based on a magnetron-sputtered Mg−Al anode [J]. Journal of Power Sources, 2022, 520: 230874.

[10] CHEN Xing-rui, ZOU Qi, SHI Zhi-ming, LE Qi-chi. ZHANG Ming-xing, ATRENS A. The discharge performance of an as-extruded Mg−Zn−La−Ce anode for the primary Mg-air battery [J]. Electrochimica Acta, 2022, 404: 139763.

[11] LI Rui-nan, LIU Qing-song, ZHANG Ru-peng, LI Ya-qi, MA Yu-lin, HUO Hua, GAO Yun-zhi, ZUO Peng-jian, WANG Jia-jun, YIN Ge-ping. Achieving high-energy-density magnesium/sulfur battery via a passivation-free Mg−Li alloy anode [J]. Energy Storage Materials, 2022, 50: 380−386.

[12] DENG Min, WANG Lin-qian, VAGHEFINAZARI B, XU Wen, FEILER C, LAMAKA S V, HÖCHE D, ZHELUDKEVICH M L, SNIHIROVA D. High-energy and durable aqueous magnesium batteries: Recent advances and perspectives [J]. Energy Storage Materials, 2021, 43: 238−247.

[13] CHEN Yu-hang, CHENG Wei-li, GU Xiong-jie, YU Hui, WANG Hong-xia, NIU Xiao-feng, WANG Li-fei, LI Hang. Discharge performance of extruded Mg−Bi binary alloys as anodes for primary Mg−air batteries [J]. Journal of Alloys and Compounds, 2021, 886: 161271.

[14] GONG Chang-wei, HE Xin-ze, FANG Da-qing, LIU Bao-sheng, YAN Xue. Effect of second phases on discharge properties and corrosion behaviors of the Mg−Ca−Zn anodes for primary Mg−air batteries [J]. Journal of Alloys and Compounds, 2021, 861: 158493.

[15] DENG Min, WANG Lin-qian, HÖCHE D, LAMAKA S V, SNIHIROVA D, JIANG Ping-li, ZHELUDKEVICH M L. Corrosion and discharge properties of Ca/Ge micro-alloyed Mg anodes for primary aqueous Mg batteries [J]. Corrosion Science, 2020, 177: 108958.

[16] MALYI O I, TAN T L, MANZHOS S. In search of high performance anode materials for Mg batteries: Computational studies of Mg in Ge, Si, and Sn [J]. Journal of Power Sources, 2013, 233: 341−345.

[17] GU Xiong-jie, CHENG Wei-li, CHENG Shi-ming, LIU Yan-hui, WANG Zhi-feng, YU Hui, CUI Ze-qin, WANG Li-fei, WANG Hong-xia. Tailoring the microstructure and improving the discharge properties of dilute Mg−Sn−Mn−Ca alloy as anode for Mg−air battery through homogenization prior to extrusion [J]. Journal of Materials Science & Technology, 2021, 60: 77−89.

[18] WANG Wan, LIU Jing-jing, WU Tian-qi, MAO Ting-xin, CHEN Jin-peng, ZHANG Wei-cheng, SHI Zhi-cong, WANG Nai-guang. Micro-alloyed Mg−Al−Sn anode with refined dendrites used for Mg-air battery [J]. Journal of Power Sources, 2023, 583: 233569.

[19] CHEN Xi-ze, WEI Shang-hai, TONG Fang-lei, TAYLOR M P, CAO Peng. Electrochemical performance of Mg−Sn alloy anodes for magnesium rechargeable battery [J]. Electrochimica Acta, 2021, 398: 139336.

[20] LIU Hong-mei, CHEN Yun-gui, TANG Yong-bai, WEI Shang-hai, NIU Gao. Tensile and indentation creep behavior of Mg−5%Sn and Mg−5%Sn−2%Di alloys [J]. Materials Science and Engineering: A, 2007, 464(1/2): 124−128.

[21] YU Kun, XIONG Han-qing, WEN Li, DAI Yi-long, YANG Shi-hai, FAN Su-feng, TENG Fei, QIAO Xue-yan. Discharge behavior and electrochemical properties of Mg−Al−Sn alloy anode for seawater activated battery [J]. Transactions of Nonferrous Metals Society of China, 2015, 25: 1234−1240.

[22] CHEN Xing-rui, ZOU Qi, LE Qi-chi, ZHANG Ming-xing, LIU Ming, ATRENS A. Influence of heat treatment on the discharge performance of Mg−Al and Mg−Zn alloys as anodes for the Mg-air battery [J]. Chemical Engineering Journal, 2022, 433: 133797.

[23] GO J B, LEE J U, YU H, PARK S H. Influence of Bi addition on dynamic recrystallization and precipitation behaviors during hot extrusion of pure Mg [J]. Journal of Materials Science & Technology, 2020, 44(9): 62−75.

[24] SONG Guang-ling, UNOCIC K A, The anodic surface film and hydrogen evolution on Mg [J]. Corrosion Science, 2015, 98: 758−765.

[25] SONG Dan, MA Ai-bin, JIANG Jing-hua, LIN Ping-hua, YANG Dong-hui, FAN Jun-feng. Corrosion behavior of equal-channel-angular-pressed pure magnesium in NaCl aqueous solution [J]. Corrosion Science, 2010, 52: 481−490.

[26] PUTILOVA I N, BALEZIN S A, BARANNIK V P, KING C V. Metallic corrosion inhibitors [J]. Journal of the Electrochemical Society, 1961, 108(10): 275−289.

[27] SUN Hao, SU Gui-rong, ZHANG Ya-ping, REN Ji-chang, CHEN Xiang, HOU Huai-yu, DING Zhi-gang, ZHANG Tao, LIU Wei. First-principles modeling of the anodic and cathodic polarization to predict the corrosion behavior of Mg and its alloys [J]. Acta Materialia, 2023, 244: 118562.

[28] FENG Jia-wen, LI Han-ning, DENG Kun-kun, FERNANDEZ C, ZHANG Qing-rui, PENG Qiu-ming. Unique corrosion resistance of ultrahigh pressure Mg−25Al binary alloys [J]. Corrosion Science, 2018, 143: 229−239.

[29] XU Bing-qian, SUN Jia-peng, HAN Jing, YANG Zhen-quan, ZHOU Hao, XIAO Li-rong, XU Song-song, HAN Ying, MA Ai-bin, WU Guo-song. Effect of hierarchical precipitates on corrosion behavior of fine-grain magnesium−gadolinium−silver alloy [J]. Corrosion Science, 2022, 194: 109924.

[30] YANG Zhen-quan, MA Ai-bin, XU Bing-qian, JIANG Jing-hua, SUN Jia-peng. Corrosion behavior of AZ91 Mg alloy with a heterogeneous structure produced by ECAP [J]. Corrosion Science, 2021, 187: 109517.

[31] LUO Yao-feng, DENG Yun-lai, GUAN Li-qun, YE Ling-ying, GUO Xiao-bin. The microstructure and corrosion resistance of as-extruded Mg−6Gd−2Y−(0−1.5)Nd−0.2Zr alloys [J]. Materials & Design, 2020, 186: 108289.

[32] GOMES M P, COSTA I, PÉBÈRE N, ROSSI J L, TRIBOLLET B, VIVIER V. On the corrosion mechanism of Mg investigated by electrochemical impedance spectroscopy [J]. Electrochimica Acta, 2019, 306: 61−70.

[33] DUAN Guo-qing, YANG Li-xin, LIAO Shang-ju, ZHANG Chun-yan, LU Xiao-peng, YANG Yang-ge, ZHANG Bo, WEI Yong, ZHANG Tao, YU Bao-xing, ZHANG Xiao-chen, WANG Fu-hui. Designing for the chemical conversion coating with high corrosion resistance and low electrical contact resistance on AZ91D magnesium alloy [J]. Corrosion Science, 2018, 135: 197−206.

[34] TONG Fang-lei, CHEN Xi-ze, WEI Shang-hai, MALMSTRÖM J, VELLA J, GAO Wei. Microstructure and battery performance of Mg−Zn−Sn alloys as anodes for magnesium−air battery [J]. Journal of Magnesium and Alloys, 2021, 9: 1967−1976.

[35] LIU Xuan, LIU Shi-zhe, XUE Ji-lai. Discharge performance of the magnesium anodes with different phase constitutions for Mg−air batteries [J]. Journal of Power Sources, 2018, 396: 667−674.

[36] ZENG Rong-chang, SUN Lu, ZHENG Yu-feng, CUI Hong-zhi, HAN En-hou. Corrosion and characterisation of dual phase Mg−Li−Ca alloy in Hank's solution: The influence of microstructural features [J]. Corrosion Science, 2014, 79: 69−82.

[37] PESTERFIELD L L, MADDOX J B, CROCKER M S, SCHWEITZER G K. Pourbaix (*E*−pH-M) diagrams in three dimensions [J]. Journal of Chemical Education, 2012, 89: 891−899.

[38] LIU Xian-bin, SHAN Da-yong, SONG Ying-wei, CHEN Rong-shi, HAN En-hou. Influences of the quantity of Mg_2Sn phase on the corrosion behavior of Mg−7Sn magnesium alloy [J]. Electrochimica Acta, 2011, 56: 2582−2590.

[39] HÖCHE D. Simulation of corrosion product deposit layer growth on bare magnesium galvanically coupled to aluminum [J]. Journal of the Electrochemical Society, 2015, 162(1): C1−C11.

[40] READ W T, SHOCKLEY W. Dislocation models of crystal grain boundaries [J]. Physical Review Letters, 1950, 78(3): 275−289.

[41] GUO Fei, ZHANG Ding-fei, YANG Xu-sheng, JIANG Lu-yao, CHAI Sen-sen, PAN Fu-sheng. Effect of rolling speed on microstructure and mechanical properties of AZ31 Mg alloys rolled with a wide thickness reduction range [J]. Materials Science and Engineering: A, 2014, 619: 66−72.

[42] SHANGGUAN Fei-er, CHENG Wei-li, CHEN Yu-hang, YU Hui, WANG Li-fei, LI Hang, WANG Hong-xia, WANG Jin-hui. Elucidating the dependence of electrochemical behavior and discharge performance on the grain structure of lean Mg−0.3Bi−0.3Ag−0.3In anodes in primary Mg-air battery [J]. Journal of Power Sources, 2023, 564: 232856.

[43] HOPKINS B J, SHAO-HORN Y, HART D P. Suppressing corrosion in primary aluminum–air batteries via oil displacement [J]. Science, 2018, 362(6415): 658−661.

[44] WU Zi-bin, ZHANG Hai-tao, ZHENG Yu-qian, ZOU Jing, YANG Dong-hui, GUO Cheng, QIN Ke, BAN Chun-yan, CUI Jian-zhong, NAGAUMI H. Electrochemical behaviors and discharge properties of Al−Mg−Sn−Ca alloys as anodes for Al−air batteries [J]. Journal of Power Sources, 2021, 493: 229724.

[45] WU Zi-bin, ZHANG Hai-tao, TANG Shuai, ZOU Jing, YANG Dong-hui, WANG Ye-qing, QIN Ke, BAN Chun-yan, CUI Jian-zhong, NAGAUMI H. Effect of calcium on the electrochem

[46] ical behaviors and discharge performance of Al−Sn alloy as anodes for Al–air batteries [J]. Electrochimica Acta, 2021, 370: 137833.

[47] XU Ting, HU Zheng-fei, YAO Cheng. The effects of Ca addition on corrosion and discharge performance of commercial pure aluminum alloy 1070 as anode for Aluminum-air battery [J]. International Journal of Electrochemical Science, 2019, 14: 2606−2620.
[48] WU Zi-bin, ZHANG Hai-tao, NAGAUMI H, WANG Dong-tao, LUO Shun-cun, DONG Xin, ZOU Jing, YANG Dong-hui, CUI Jian-zhong. Effect of microstructure evolution on the discharge characteristics of Al−Mg−Sn-based anodes for Al−air batteries [J]. Journal of Power Sources, 2022, 521: 230928.

镁空气电池用无析出相轧制在 Mg−Sn 合金阳极材料的电化学行为及放电性能

李 旭[1]，程伟丽[1,2]，李 戬[2]，上官菲儿[1]，余 晖[3]，
王利飞[1]，李 航[1]，王红霞[1]，王金辉[2]，侯 华[4]

1. 太原理工大学 材料科学与工程学院，太原 030024；
2. 青海大学 盐湖化工综合研究中心开放项目，西宁 810016；
3. 河北工业大学 材料科学与工程学院，天津 300132；
4. 中北大学 材料科学与工程学院，太原 030051

摘 要：在 573 K 下通过轧制成功制备一种具有均匀等轴晶粒结构的新型无析出相 Mg−0.1Sn 阳极材料。电化学测试结果表明，Mg−0.1Sn 合金表现出较强的阳极溶解动力学。用该阳极组装的镁空气电池在 0.5 mA/cm^2 时的放电电压为 1.626 V，在 10 mA/cm^2 时阳极效率为 58.17%，能量密度为 1730.96 mW/h。这种性能归因于阳极表面充足的有效反应面积抑制了块效应，以及由于均匀的基面织构而减弱了自腐蚀。

关键词：Mg 空气电池；Mg−Sn 阳极；晶粒结构；电化学行为；放电性能

(Edited by Xiang-qun LI)